ADVANCED ENERGY MATERIALS
www.advenergymat.de

Solid Electrolyte Interface Regulated by Solvent-in-Water Electrolyte Enables High-Voltage and Stable Aqueous Mg-MnO_2 Batteries

Yan Xu, Zaichun Liu, Xinhua Zheng, Ke Li, Mingming Wang, Wei Yu, Hanlin Hu, and Wei Chen**

Mg batteries utilizing divalent Mg^{2+} as charge carriers have been attracting significant attention for energy storage owing to their uniqueness in terms of low cost, high safety, and high energy density. However, the short cycling life arising from the accumulation of a passivation layer on the Mg anode prohibits their further development. Here, a new strategy to suppress the accumulation of the passivation layer is presented, thus stabilizing the Mg anode by constructing a robust interfacial layer using organic solvent-in-water electrolytes. The organic solvents decompose on the Mg anode to form a MgO, polyether Mg enriched organic-inorganic hybrid interfacial layer, preventing free water attack to the Mg anode. In addition, the organic solvent forms an H-bond with H_2O to suppress the water activity and therefore protecting the Mg anode. As an illustration to benefits of the solvent-in-water electrolytes, a Mg-MnO_2 battery that is coupled by a MnO_2 cathode in Mn^{2+}/MnO_2 chemistry with the Mg anode is developed. The Mg-MnO_2 battery exhibits a well-maintained discharge plateau at ≈2.5 V and a discharging capacity of ≈500 mAh g^{-1} over 1000 cycles. This result highlights the feasibility to stabilize the Mg anode by interface engineering through the solvent-in-water electrolyte design.

1. Introduction

Lithium-ion batteries account for a large global battery market and are widely applied in portable electronics and electrified vehicles owing to their high energy density.[1] However, the growing concerns about safety issues of non-aqueous electrolytes[2] in Li-ion battery motivated us to shift from current organic electrolyte-based batteries to aqueous batteries. The electrochemical storage of Li^+,[3] Na^+,[4] K^+,[5] Mg^{2+},[6] and Zn^{2+}[7] in aqueous electrolytes have been considered as promising aqueous battery systems. However, the metallic Li, Na, and K are incompatible with aqueous electrolytes. Therefore, insertion-type compound anodes are applied in Li-, Na-, K-based aqueous batteries, which largely limited their energy densities.[8] Aqueous Zn-ion batteries are particularly attractive owing to the high water compatibility and stability of metallic Zn[7a,9] as compared to the alkali metals. Unfortunately, the Zn dendrite formation as well as limited voltage and energy density of the aqueous Zn ion batteries have prohibited their practical applications.[10] Therefore, new battery chemistries with low-cost, environmental benign, high energy density, and safety are highly desirable.

Magnesium batteries utilizing divalent Mg^{2+} as charge carriers offer significant improvements in cost, safety, working voltage, and volumetric energy density due to the unique nature of earth-abundance, dendrite-free,[11] low reduction potential (−2.37 V versus SHE), and high-capacity (3832 mAh cm^{-3}) of the metallic Mg.[12] All of these merits enable the metallic Mg a promising anode for aqueous and non-aqueous electrolytes based batteries. Over the past few decades, various cathode materials, such as MnO_2,[13] air,[14] H_2O_2,[15] have been coupled with the metallic Mg to fulfill the requirements of different battery systems. For example, when the primary Mg-MnO_2 dry cell was initially developed in the early 20th century, it has been successfully applied in military communication equipment and aircraft emergency transmitters for a long period of time due to its high theoretical energy density of 759 Wh kg^{-1}.[16] Therefore, aqueous Mg-based batteries showed great promises in some

Y. Xu, Z. Liu, X. Zheng, K. Li, M. Wang, W. Chen
Department of Applied Chemistry
School of Chemistry and Materials Science
Hefei National Laboratory for Physical Sciences at the Microscale
University of Science and Technology of China
Hefei, Anhui 230026, China
E-mail: weichen1@ustc.edu.cn

Y. Xu, H. Hu
Hoffman Institute of Advanced Materials
Shenzhen Polytechnic
Shenzhen, Guangdong 518000, China
E-mail: hanlinhu@szpt.edu.cn

W. Yu
State Key Laboratory of Catalysis
Dalian Institute of Chemical Physics
Chinese Academy of Sciences
Dalian National Laboratory for Clean Energy
Dalian, Liaoning 116023, China

The ORCID identification number(s) for the author(s) of this article can be found under https://doi.org/10.1002/aenm.202103352.

DOI: 10.1002/aenm.202103352

high-energy density demanding areas. However, the aqueous Mg batteries particularly the Mg-MnO_2 batteries have short life span due to the deactivation of the metallic Mg caused by the accumulation of $Mg(OH)_2$ passivation layer on its surface.

To date, much effort has been devoted to extending the cycle life of the Mg-MnO_2 batteries by different approaches, which are focused on the exploration of different MnO_2 structures and electrolytes. However, the reported Mg-MnO_2 batteries still suffer from critical issues of high overpotential, sloping discharge curve, fast capacity decay, low reaction kinetics, and short cycle life,[13b] which could be mainly ascribed to the accumulation of $Mg(OH)_2$ passivation layer on the Mg anode. The formation of $Mg(OH)_2$ passivation layer originates from the chemical reactions of Mg anode with electrolyte. Mg anode tends to react chemically with water vigorously in aqueous electrolyte because the standard potential of Mg^{2+}/Mg is as low as −2.37 V (versus SHE). Coating Mg surface with an artificial interface provides a feasible approach to the remission of the $Mg(OH)_2$ passivation layer. For example, it was reported that an artificial interface originating from the decomposition of fluorinated ether could enable graphite or Li-metal cycling in aqueous electrolyte.[1]

Here we report a strategy to overcome the challenges of $Mg(OH)_2$ passivation layer accumulation by using an organic solvent-in-water (SIW) electrolyte. The water in SIW electrolyte inherits the merits of aqueous electrolyte, such as the high ionic conductivity, environmental friendliness, and non-flammability, as well as the organic solvent that is favorable to absorb on the metallic Mg and reduce on the surface of Mg anode to form an organic-inorganic hybrid protective layer, thereby avoiding the electrical insulating $Mg(OH)_2$ accumulation. In addition, the organic solvent could bind with free water and suppress the activity of water in the aqueous electrolyte. The versatile effect of non-aqueous solvents avoids the formation of $Mg(OH)_2$ passivation layer. When metallic Mg is coupled with MnO_2 cathode in the Mn^{2+}/MnO_2 chemistry, our Mg-MnO_2 full cell shows a pronounced discharge plateau at ≈2.51 V and a discharging capacity of ≈500 mAh g^{-1} for over 1000 cycles. This study provides insights into addressing the challenges of aqueous Mg-MnO_2 batteries for practical energy storage applications.

2. Results and Discussion

2.1. Charge Storage Mechanism and Properties of the SIW Electrolytes

As schematically depicted in **Figure 1**a, the Mg-MnO_2 full cell is composed of a cathode-less porous carbon felt, a metallic Mg anode, and saturated Mg^{2+} and Mn^{2+} in a mixture of organic solvent with water as the SIW electrolyte. $MgCl_2$ is selected as the soluble salt due to its high solubility in water (≈7.8 M at room temperature, which can be obtained from the Table of Solubility). When charging the Mg-MnO_2 cell, soluble Mn^{2+} ions in the electrolyte diffuse to the cathode and deposit as solid MnO_2 on the carbon felt. During discharge of the battery, the as-deposited MnO_2 on the cathode is dissolved back

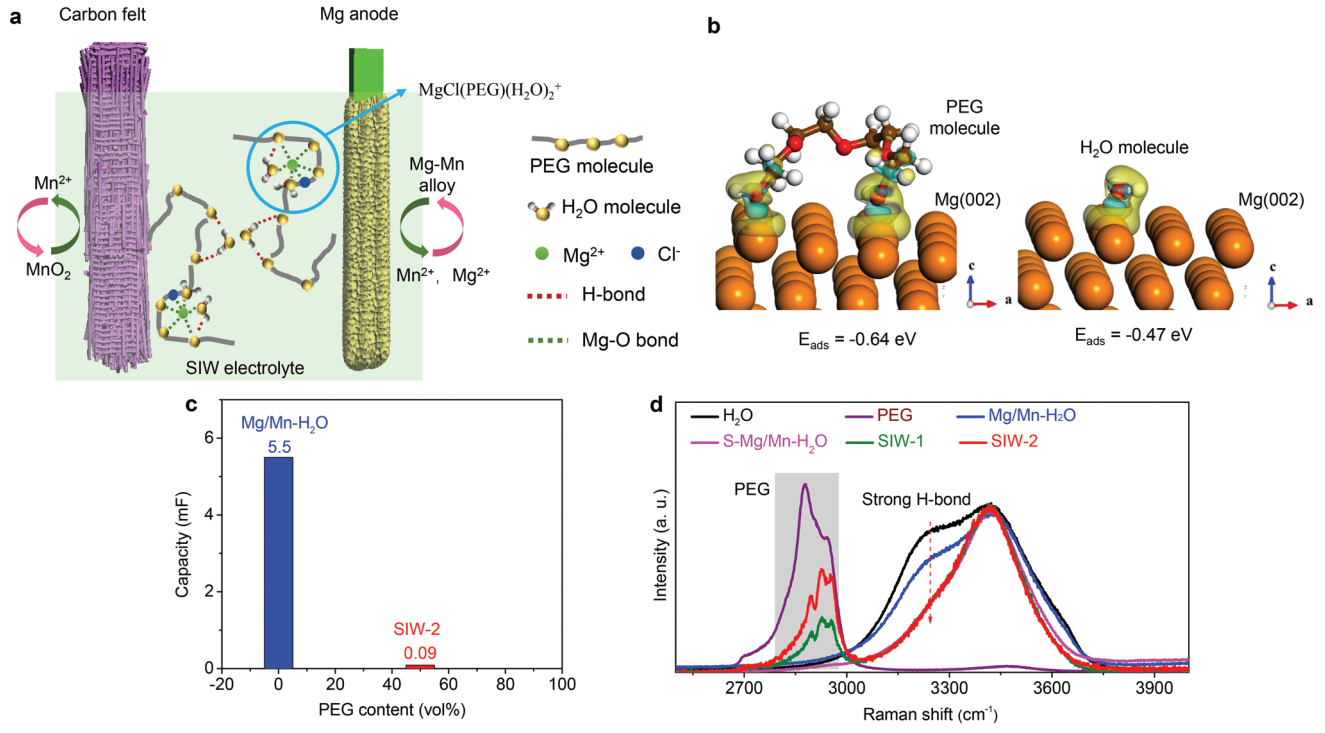

Figure 1. Working mechanism of Mg-MnO_2 battery and properties of the SIW electrolyte. a) A schematic illustration of the Mg-MnO_2 battery in the charge and discharge modes. b) Calculations of the absorption energy of PEG and water on Mg(002) surface. c) The double layer capacitance in SIW-2 and Mg/Mn-H_2O electrolytes. d) Raman spectra of a O—H stretching vibration of different electrolytes. SIW-2 and Mg/Mn-H_2O stand for saturated $MgCl_2$-1 M $MnCl_2$ in H_2O:PEG = 1:1 and 1 M $MgCl_2$-1 M $MnCl_2$ electrolytes, respectively.

to soluble Mn^{2+} in electrolyte. The anode is operated by the deposition/stripping of Mg-Mn alloy, which was verified via CV in a three-electrode cell as shown in Figure S1, Supporting Information. X-ray diffraction (XRD) was conducted to show the Mg-Mn alloy patterns (Figure S2, Supporting Information), which confirms the formation of the Mg-Mn alloy. Further, the anode was characterized by SEM after the Mg-Mn alloy deposition. As shown in Figure S3, Supporting Information, the Mg-Mn alloy was uniformly deposited, which is consistent with the TEM and EDX mapping tests (Figure S4, Supporting Information). For the SIW electrolyte, organic solvents with O, F, Cl can be chosen, which is able to absorb on the Mg anode and form H-bond with H atoms in the water. Dissolution of $MgCl_2$ into the mixed solvents to saturated concentrations leads to further decrease of the activity of water, forming the SIW electrolytes, as shown in Figure 1a. To demonstrate the design principle of the electrolytes, polyethylene glycol (PEG) was chosen as the model solvent to formulate the SIW electrolyte thanks to its water-miscible, non-toxic, and low-cost features. It is worth noting that ethylene glycol (EG), polyethylene oxide (PEO), polyvinyl alcohol (PVA), polyacrylonitrile (PAN), tetraglyme as solvents can also potentially be applied to our Mg-MnO_2 cells. We use PEG in this work as a demonstration of the battery concept unless otherwise specified.

To demonstrate the effect of PEG, a series of *x*PEG-(1-*x*) H_2O solvents with saturated $MgCl_2$ and 1 M $MnCl_2$ were prepared with the PEG content (*x*) ranging from 0% to 50%. First, the absorption energy of PEG and water on Mg(002) surface was evaluated by DFT calculation. As shown in Figure 1b, the absorption energies of PEG and water on Mg(002) surface are −0.64 and −0.47 eV, respectively, which indicates that PEG is more favorable to absorb on the Mg(002) surface than water. To investigate the change of interfacial properties by the introduction of PEG, cyclic voltammetry (CV) under various scan rates (Figure S5, Supporting Information) was conducted. As shown in Figure 1c and Figure S5, Supporting Information, the double layer capacitance in the SIW-2 (saturated $MgCl_2$-1 M $MnCl_2$ in H_2O:PEG = 1:1) electrolyte is negligible (0.09 mF) as compared to that in Mg/Mn-H_2O (1 M $MgCl_2$-1 M $MnCl_2$ in H_2O) electrolyte (5.5 mF), which indicated that a better interface can be constructed due to the absorption of PEG on the Mg anode. This is helpful to shield water to attack Mg anode.

To get a better understanding on the electrolyte properties, the electrolyte structure was analyzed via Raman combined with computation. First, PEG and water interaction was analyzed by Raman in the solvent of H_2O:PEG = 1:1 (vol%). The O—H stretching vibration of water molecules (3000–3700 cm^{-1}) can be deconvoluted into three components located at ≈3260, ≈3495, and ≈3702 cm^{-1} (Figure S6, Supporting Information), which correspond to the water molecules with strong, weak, and non H-bonds, respectively. As shown in Figure S7, Supporting Information, the strong H-bond decreased after PEG was added into water, which indicated that PEG could break the strong H-bond network (O···H—O) in water. The reduced H bond network of water molecules could decrease the transport of proton[17] and hydroxide[18] ions through the Grotthuss diffusion mechanism. In addition, the O—H stretching mode shifts to higher wavenumber upon adding PEG. This blue shift can be attributed to the interaction between H of the O—H bond in water molecules and O of the C—O bond in PEG (C—O···H—O). Further, the solvation structure of $MgCl_2$ in the solvents of H_2O and H_2O:PEG = 1:1(vol%) have been calculated (Figure S8, Supporting Information). It showed that $Mg(H_2O)_6^{2+}$ and $Mg(PEG)(H_2O)_2Cl^+$ cations are the most possible cations in these two solutions and the binding energies of $Mg(H_2O)_6^{2+}$ and $Mg(PEG)(H_2O)_2Cl^+$ cations are −15.15 and −25.28 eV, respectively, which indicated the preferential solvation of PEG with Mg^{2+}. The altered Mg^{2+} solvation sheath by O-containing organic solvent is favorable for the suppression of water decomposition[19] and the regulating cation concentration in the vicinity of anode.[20] In addition, improving the salt concentration could destruct the strong H-bond further. As shown in Figure 1d, with the salt concentration increased, the strong H-bond peak (3260 cm^{-1}) in the Raman spectra decreased gradually, indicating that the water activity is highly suppressed and less free water is existed in the electrolyte with increasing of the salt concentration. As such, the optimal SIW electrolyte is expected to improve the electrochemical performance of the aqueous Mg-MnO_2 batteries.

The chemical and physical properties of the SIW electrolytes were further evaluated. The electrochemical stability windows of the electrolytes, which depend on the hydrogen evolution reaction (HER) and oxygen evolution reaction (OER), were determined by linear sweep voltammetry (LSV). As shown in **Figure 2**a, the HER and OER stability windows in the electrolyte of 1 M $MgCl_2$ in H_2O are 1.42 and 2.6 V (versus Mg^{2+}/Mg), respectively, which can be expanded by the introduction of PEG into the electrolyte. As the PEG concentration increased to 50% by the volume, the HER and OER stability windows in the electrolyte of saturated $MgCl_2$ in H_2O can reach as low as 0.45 V and as high as 2.8 V (versus Mg^{2+}/Mg), respectively, indicating the protective effect of SEI on the Mg anode. It was worth to mention that strong peaks appeared around hydrogen evolution potentials in the electrolytes of 1 M $MgCl_2$ in H_2O and saturated $MgCl_2$ in H_2O, which can be ascribed to the formation of $Mg(OH)_2$ component due to the decomposition of water on the Mg anode. While no peaks can be observed around hydrogen evolution potentials with the addition of PEG, suggesting the suppressed water decomposition on Mg anode with the introduction of PEG. In addition, with the PEG content increased in the electrolyte of saturated $MgCl_2$ in H_2O, the OER current density decreased significantly beyond 2.8 V (versus Mg^{2+}/Mg), which further suggested that the water activity has been decreased. The electrolyte stability window test results demonstrate the importance of the electrolyte regulation by the application of PEG as a solvent-in-water electrolyte to achieve stable operation of Mg anode. Furthermore, the Mg‖Mg symmetric cells in Mg/Mn-H_2O and SIW-2 electrolytes were cycled at the current density of 1 mA cm^{-2} to testify their stabilities. As shown in Figure 2b, the polarization voltage of the Mg‖Mg cell in the electrolyte of Mg/Mn-H_2O increased gradually and reached 1.8 V. In contrast, the polarization voltage of the Mg‖Mg cell in the electrolyte of SIW-2 can be stabilized around 0.03 V over 750 min. This result indicated that the $Mg(OH)_2$ passivation layer accumulated rapidly in the electrolyte of Mg/Mn-H_2O, while a stabilized interfacial layer formed in the electrolyte of SIW-2. PEIS was conducted to Mg‖Mg symmetric

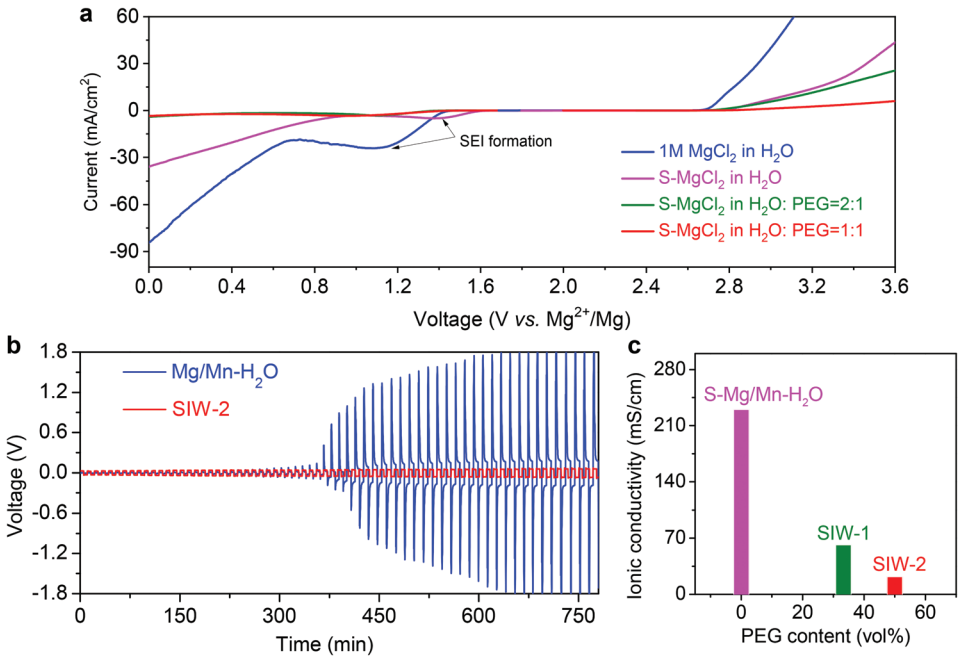

Figure 2. The physical and chemical properties of different electrolytes. a) Electrochemical stability windows of 1 M $MgCl_2$ in H_2O, saturated $MgCl_2$ in H_2O, saturated $MgCl_2$ in H_2O:PEG = 2:1, and saturated $MgCl_2$ in H_2O:PEG = 1:1 electrolytes determined by LSV tests on Pt foil at a scan rate of 10 mV s^{-1}. b) Cycling stability of Mg||Mg symmetric cell in the electrolytes of Mg/Mn-H_2O and SIW-2 at the current density of 1 mA cm^{-2}. c) Ionic conductivity of S-Mg/Mn-H_2O, SIW-1, and SIW-2 electrolytes.

cells in the electrolytes of Mg/Mn-H_2O and SIW-2. As shown in Figure S9, Supporting Information, although the interfacial impedance of Mg||Mg symmetric cells was lower in the electrolytes of Mg/Mn-H_2O at the first several cycles, it was significantly increased to thousands of ohms at the 85th cycle, which resulted in the failure of the cell. The impedance of Mg||Mg symmetric cells in the electrolyte of SIW-2 was also increased with cycle number due to the formation of interfacial layer on the freshly deposited Mg, while its impedance increase was much slower, which indicated a relatively stabilized interfacial layer that has been constructed in the electrolyte of SIW-2. The ionic conductivity of different electrolytes was tested and calculated by the impedance spectra in stainless steel (SS)||SS symmetric cells at ambient temperature (Figure S10, Supporting Information). It revealed that the ionic conductivities of the electrolytes ranged from 230 to 21.8 mS cm^{-1} with PEG content increased from 0 to 50 vol% (Figure 2c), which is comparable to that of the water-in-salt electrolytes.[21]

2.2. Electrochemical Performance of Mg-MnO_2 Cell

In light of the proposed energy storage mechanism and the designed electrolytes, we constructed the Mg-MnO_2 full cell and tested its electrochemical performance at room temperature. An optimal voltage of 2.8 V was applied to charge the cell to avoid the OER on the cathode, and it was then galvanostatically discharged to 1.4 V. As shown in **Figure 3**a, the cells in the control electrolyte of Mg/Mn-H_2O showed a discharge plateau at ≈2.61 V with a discharge capacity of ≈440 mAh g^{-1} (based on the mass of MnO_2 on the cathode) at the first cycle. While in the subsequent cycles, the discharge plateau became much shorter and the plateau voltage decayed from ≈2.61 to ≈2.48 V at the eighth cycle and disappeared afterward, resulting in the negligible discharge capacity from the ninth cycle. In addition, increasing voltage dips can be observed at the beginning of each discharge process from the second cycle. In order to figure out origin of the voltage dip, three-electrode test was conducted by using carbon felt as working electrode, Mg foil as counter electrode, and Ag/AgCl as reference electrode. As shown in Figure S11, Supporting Information, the cathode displayed an excellently retained plateau around 1 V, which matches very well with the redox potential of typical Mn^{2+}/MnO_2 reactions and confirms good reversibility of the MnO_2 cathode. However, intensively increased voltage dips can be observed within only the first five cycles on the Mg anode, which indicated that the voltage decay of the Mg-MnO_2 cell in Mg/Mn-H_2O electrolyte is originated from the Mg anode. Therefore, the battery electrolyte needs to be modified to form a robust solid electrolyte interface on the Mg anode.

We have conducted systematical experiments on the tuning of electrolyte in order to improve the electrochemical performance of the Mg-MnO_2 cell. First, we increased the salt concentration to be saturated, and found that the specific capacity of the Mg-MnO_2 cell shrunk to 345 mAh g^{-1} and cycle life was shortened to only 6 cycles, which were triggered off by the decreased ionic conductivity of the Mg/Mn-H_2O electrolyte (Figure 3b). When 33 vol% of PEG was further introduced into the electrolyte of saturated Mg/Mn in water (referred to as SIW-1 electrolyte), the battery electrochemical performance was largely improved. Specifically, the discharge plateau was maintained at 2.5 V, and the specific capacity was increased to ≈500 mAh g^{-1} (Figure 3c). In addition, the big dip at the

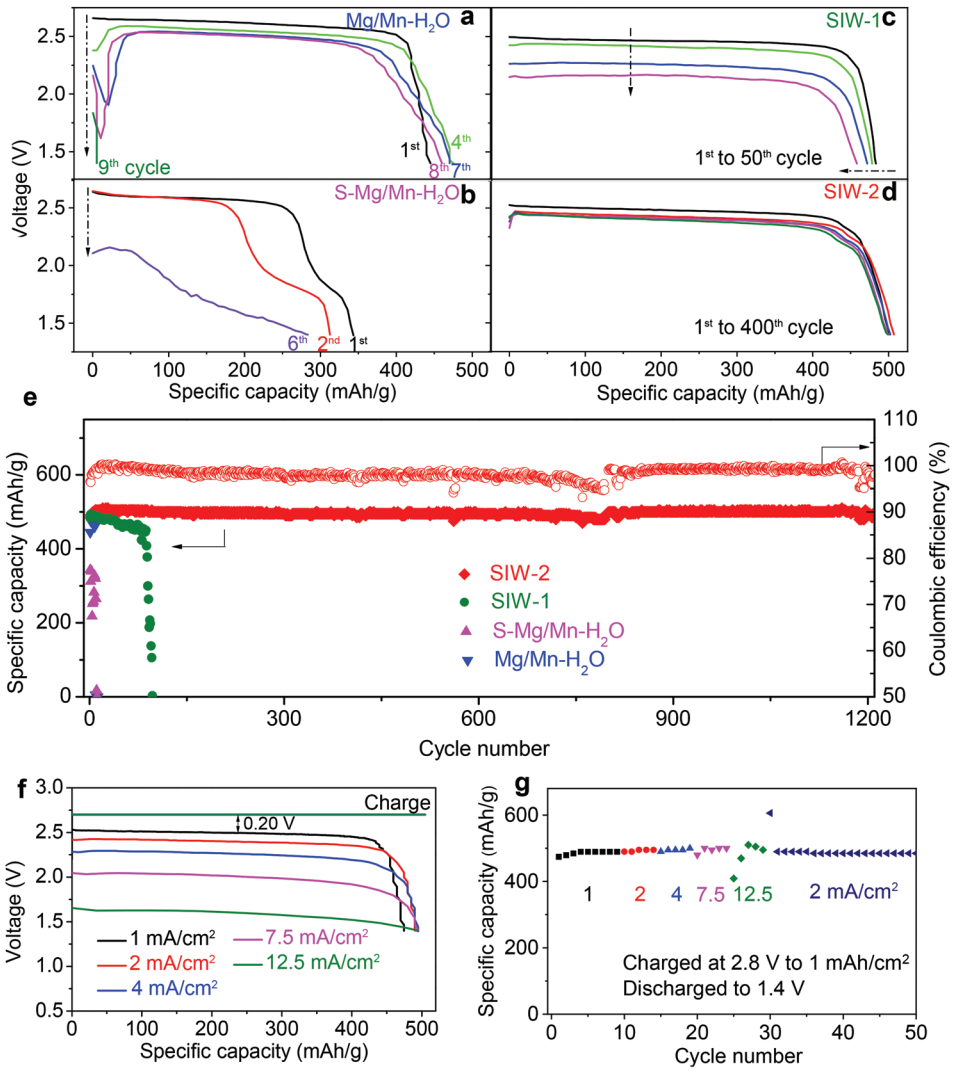

Figure 3. The electrochemical performance of Mg-MnO_2 battery in different electrolytes. a–d) The discharge behavior of Mg-MnO_2 cell in the electrolyte of Mg/Mn-H_2O, S-Mg/Mn-H_2O, SIW-1, and SIW-2 at 5C, respectively. e) Cycling stability of Mg-MnO_2 cells in different electrolytes at 5C. f) Voltage profile of Mg-MnO_2 cells in the SIW-2 electrolyte under current densities from 1 to 12.5 mA cm^{-2}. g) Rate capability of Mg-MnO_2 cells in the SIW-2 electrolyte.

beginning of discharging process disappeared, which indicated that a better solid electrolyte interface was formed to allow Mg^{2+} transfer smoothly. However, the discharge voltage and capacity still decayed gradually from 2.5 V to 2.16 V within 50 cycles in the electrolyte of SIW-1, which may be due to the attack of part of free water to the Mg anode. When the PEG content was further increased to 50 vol% in the electrolyte of saturated Mg/Mn in water (referred to as SIW-2 electrolyte), the battery electrochemical performance was significantly improved. The ultra-flat discharge plateau at a voltage of 2.5 V was maintained very well within 400 cycles, and the specific capacity was up to 500 mAh g^{-1} (Figure 3d), which is higher than that in the Mg/Mn-H_2O, S-Mg/Mn-H_2O, and SIW-1 electrolytes. In addition, stable cycling at 5 C for over 1000 cycles with around 99% capacity retention can be achieved in the electrolyte of SIW-2 (Figure 3e), which is among the most stable Mg-based battery (Table S1, Supporting Information).[22] This improved electrochemical performance and stability of Mg-MnO_2 cells were enabled by the robust solid electrolyte interface on Mg anode. Figure 3f showed the rate performance of Mg-MnO_2 cell in the electrolyte of SIW-2. We found the overpotential is only 0.20 V at the current density of 1 mA cm^{-2}. It is worth to mention that even the discharge current density increased to 12.5 mA cm^{-2}, the discharge plateau still kept at ≈1.62 V and the discharge capacity can be well maintained at nearly 500 mAh g^{-1} (Figure 3g), exhibiting a remarkable rate capability. This result indicates that the formed solid electrolyte interface in SIW-2 electrolyte enables the Mg^{2+} ions transfer smoothly even at high current density. Further increase of PEG content in the electrolyte induced too low ionic conductivity that caused sluggish reaction kinetics. Therefore, the SIW-2 electrolyte was explored as optimal in this study. In order to demonstrate generality of the regulation effect of the solvent-in-water electrolyte strategy, we also tested the Mg-MnO_2 full cell in the solvent of EG. When employing the electrolyte of saturated Mg/Mn in mixture of H_2O and EG with volume ratio of 1:1, a maintained discharge plateau at 2.5 V and long cycling life beyond 350 cycles can be achieved (Figure S12, Supporting Information), which confirmed that this electrolyte

regulation approach can be treated as a general method to different battery chemistries.

2.3. Characterizations of the Interfacial Layer of Mg Anode in SIW-2

To gain a deeper insight into the components of interfacial layers in different electrolytes, the compositions of the interfacial layers on the cycled Mg anode were analyzed using Fourier transform infrared (FTIR), XRD, and X-ray photoelectron spectroscopy (XPS). As shown in **Figure 4**a, a sharp and intense peak at 3701 cm^{-1} and a broad peak at 3437 cm^{-1} of the cycled Mg anode in the electrolyte of Mg/Mn-H_2O can be observed, which are associated with the stretching vibration of −OH group in $Mg(OH)_2$.[23] The absorption band around 572 cm^{-1} is also characteristic of $Mg(OH)_2$. The IR bands of $MgCO_3$ and

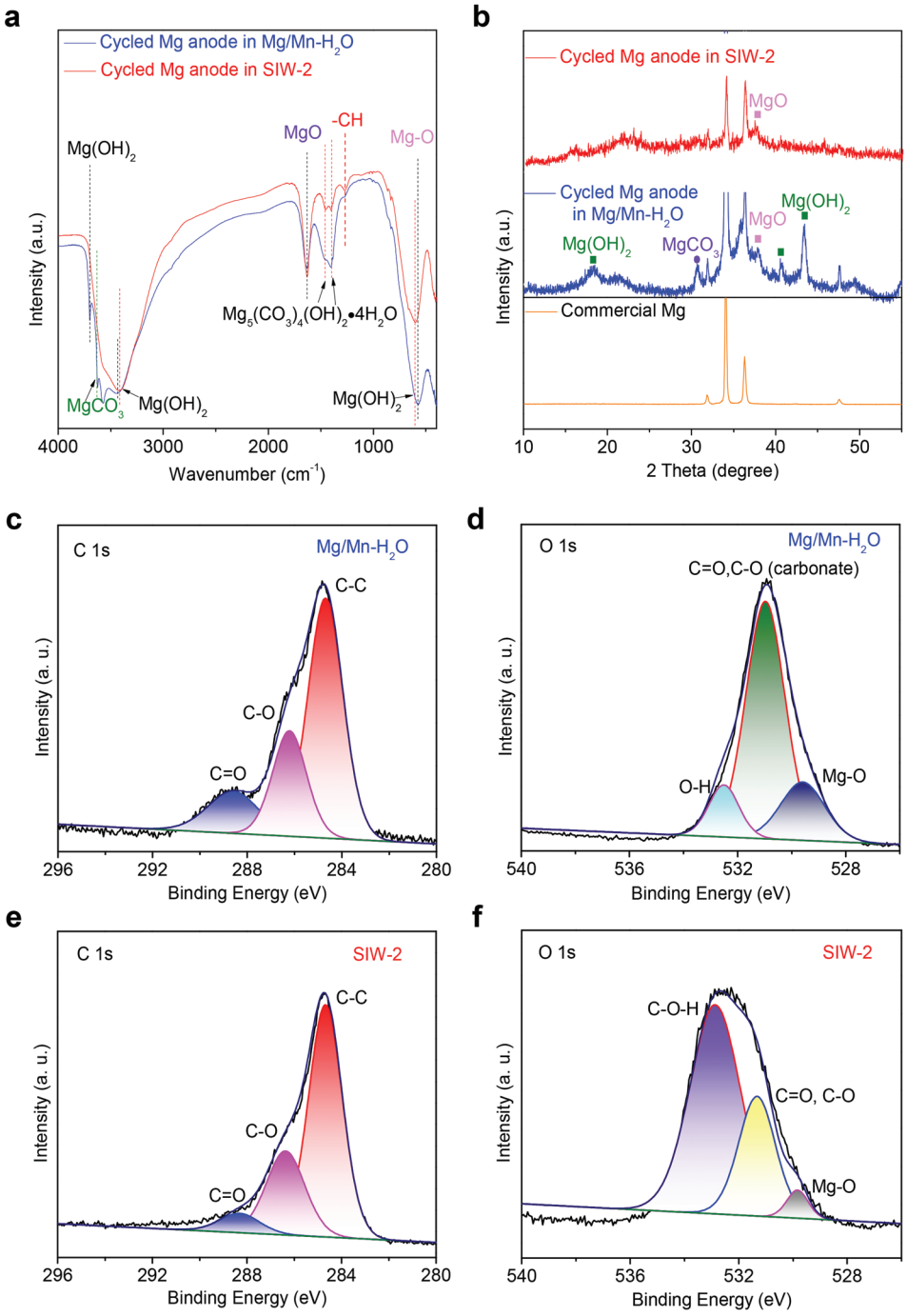

Figure 4. Characterizations of Mg-MnO_2 cells. a) FTIR of cycled Mg anode in the electrolytes of Mg/Mn-H_2O and SIW-2. b) XRD patterns of cycled Mg anode in the electrolytes of Mg/Mn-H_2O and SIW-2. c–f) XPS characterization of the passivation layer formed on the cycled Mg anode in the electrolytes of Mg/Mn-H_2O and SIW-2. The C 1s and O 1s spectra are displayed.

MgO are appeared at 3627 cm^{-1} and 1638 cm^{-1}, respectively. $Mg(OH)_2$ was obtained from the reaction between metallic Mg and H_2O, MgO may come from the reaction between the dissolved O_2 and metallic Mg, and $MgCO_3$ was from the reaction between the chemisorbed CO_2 and MgO.[23] In addition, the IR bands at 1458 and 1403 cm^{-1} can be ascribed to the component of $Mg_5(CO_3)_4(OH)_2{\bullet}4H_2O$ (Database of ATR-FT-IR). Therefore, inorganic components of MgO, $Mg(OH)_2$, $MgCO_3$, and $Mg_5(CO_3)_4(OH)_2{\bullet}4H_2O$ were the main compositions in the interfacial layer of the cycled Mg anode in the electrolyte of Mg/Mn-H_2O, which is consistent with previously reported literature.[24] Compared with the cycled Mg anode in the electrolyte of Mg/Mn-H_2O, no $Mg(OH)_2$ or $MgCO_3$ components can be detected by FTIR on the cycled Mg anode in the electrolyte of SIW-2. Instead, organic components of -OH (3438 cm^{-1}), -CH group (1264 cm^{-1}),[25] and the bond between Mg^{2+} and O atom (604 cm^{-1}) were shown, which may come from the decomposition reaction between metallic Mg and $H[OCH_2CH_2]_nOH$ (PEG molecules).

Inorganic components, such as MgO and a small amount of $Mg_5(CO_3)_4(OH)_2{\bullet}4H_2O$, can also be observed. The absorption intensity of MgO was much stronger on the cycled Mg anode in the electrolyte of SIW-2 than that in the electrolyte of Mg/Mn-H_2O, which indicated decomposition reaction between Mg and $H[OCH_2CH_2]_nOH$ contributed partially to MgO in addition to the reaction between the dissolved O_2 with Mg. It is worth noting that the absorption intensity of $Mg_5(CO_3)_4(OH)_2{\bullet}4H_2O$ on the cycled Mg anode in the electrolyte of SIW-2 was lower than that in the electrolyte of Mg/Mn-H_2O, which indicated the suppressed simultaneous reaction between H_2O, CO_2, and Mg in the electrolyte of SIW-2. In the interfacial layer of cycled Mg anode in the electrolyte of SIW-2, organic and inorganic components were included, in which inorganic components of $Mg_5(CO_3)_4(OH)_2{\bullet}4H_2O$ and MgO, have low solubility in water, which can form a stable protective layer on Mg anode. In addition, the organic protective layer of polyether was more intact,[26] which can more effectively protect Mg anode. XRD results demonstrated that in the Mg/Mn-H_2O electrolyte, inorganic byproducts of $Mg(OH)_2$, $MgCO_3$, and MgO were formed on the cycled Mg surface due to the reaction of free water with Mg anode (Figure 4b), which is consistent with the FTIR results. While in the electrolyte of SIW-2, no $Mg(OH)_2$ or $MgCO_3$ inorganic byproducts can be detected by XRD, and only MgO can be detected, which was identical with the FTIR results. XRD results indicated that the water activity has been suppressed in the PEG-containing electrolyte, leading to no $Mg(OH)_2$ byproducts formed in the interfacial layer. XPS spectra obtained for the surface components of Mg anode after 2 cycles in the electrolytes of SIW-2 and Mg/Mn-H_2O are shown in Figure 4c–f. The C 1s signal can be deconvoluted into C=O group (288.8 eV), C—O group (286.5 eV), and C-C group (284.8 eV)[27] (Figure 4c,e). The C=O and C—O groups can be detected on Mg anode in the electrolytes of Mg/Mn-H_2O, which indicated that carbonate or carbonyl group was formed on Mg anode. The carbonate group also could be detectable in O 1s spectra (531.2 eV). In addition, metal oxide (Mg-O, 530 eV) and hydroxyl (O-H, 532.5 eV) species were detectable (Figure 4d), which indicated that inorganic $MgCO_3$, $Mg(OH)_2$, and MgO were the main components on Mg anode in the electrolyte of Mg/Mn-H_2O. While in the electrolyte of SIW-2, the components in the interfacial layer showed that only carbonyl and ether groups (531.2 eV) and organic hydroxyl group (532.9 eV) can be detected from O 1s spectra, which is different from that in the Mg/Mn-H_2O electrolyte (Figure 4f). The FTIR, XRD, and XPS results of the Mg anode further indicated that both inorganic components in a composition of MgO and $Mg_5(CO_3)_4(OH)_2{\bullet}4H_2O$ as well as organic component in a composition of polyether are contained in the interfacial layer with PEG addition. This hybrid interfacial layer is able to more effectively block the attack of water to Mg anode, which is beneficial to the stability of Mg-MnO_2 full cell. We also investigated the morphology and structural evolution of the Mg anode by SEM. The pristine Mg anode showed relatively flat surface morphology (Figure S13, Supporting Information), and the cycled Mg anode in the SIW-2 electrolyte showed a dendrite-free morphology, which guaranteed the safety of the Mg-MnO_2 cells.

Moreover, the morphology and components of the MnO_2 cathode were analyzed. SEM images showed that, compared to the clean surface of pristine carbon felt (Figure S14a, Supporting Information), the carbon felt (CF) cathode after the first charge to 5 mAh was covered with a discrete layer of MnO_2 nanoparticles (Figure S14b, Supporting Information). To figure out the compositions of deposited products on CF, XRD was first conducted. As shown in Figure S14c, Supporting Information, weak MnO_2 peak positioned at 36.7° can be observed, suggesting that the deposited MnO_2 has poor crystalline structure. The polycrystalline nature of the deposited MnO_2 is more favorable for its completely dissolution during cell discharge. Therefore, we further conducted FTIR and XPS to confirm the deposited MnO_2. As shown in Figure S14d, Supporting Information, the peaks appeared around 3430 and 1640 cm^{-1} can be ascribed to the stretching and bending vibration of the hydroxyl group of Mn—OH and H—O—H, respectively. The peaks positioned at 1407 and 572 cm^{-1} are attributed to the vibrations of the O—Mn—O and O—Mn bonds of MnO_2, respectively. To evaluate the oxidation state of the deposited MnO_2, we have performed XPS measurements on the cathode at the charged and discharged states. After charging to 5 mAh, the cathode shows a pronounced MnO_2 peak located at 641.8 eV in Mn 2p spectroscopy, which is completely disappeared at the fully discharged state (Figure S14e, Supporting Information). The core-level spectra of Mn 3s were utilized to determine the manganese oxidation states as suggested previously.[28] In the case of the cathode at its charged state, the average oxidation state of MnO_2 was calculated to be 3.64 on the basis of the Mn 3s peak splitting energy of 4.7 eV (Figure S14f, Supporting Information). Therefore, the actual electron charge transfer number in the Mn^{2+}/MnO_2 cell is 1.64, corresponding to a specific capacity of 505 mAh g^{-1}. The actual reaction on the cathode is $Mn^{2+} + 1.82\ H_2O = MnO_{1.82} + 3.64\ H^+ + 1.64\ e^-$.

2.4. Scale-Up of Mg-MnO_2 Cell

To increase the cell capacity for large-scale energy storage applications, we have scaled up the energy storage capacity of the Mg-MnO_2 cell by amplifying the surface area of CF cathode and Mg anode area (6 × 9 cm^2). When charging the battery to 50 mAh, the large Mg-MnO_2 cells delivered

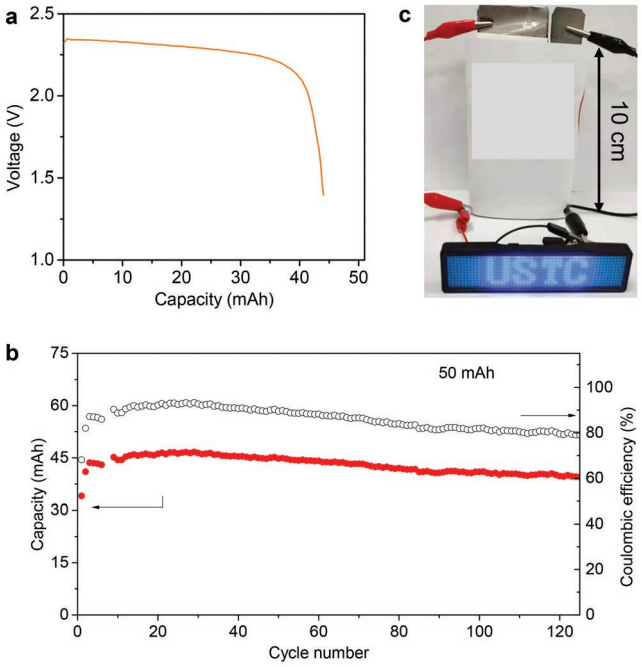

Figure 5. Scale-up of the Mg-MnO_2 battery and its electrochemical performance. a) Voltage profile of the scaled-up Mg-MnO_2 cell by charging to 50 mAh. b) Cycle stability and Coulombic efficiency of the scaled-up Mg-MnO_2 battery by charging to 50 mAh. c) Digital photograph of the LED lighting by the scaled-up Mg-MnO_2 battery.

42 mAh discharge capacity and the corresponding CE was up to ≈84%. The scaled-up Mg-MnO_2 battery showed a discharge plateau of 2.39 V (**Figure 5**a) together with a relatively stable cycle life of more than 100 cycles (Figure 5b), which is reasonable for practical application. The discharge plateau and Coulombic efficiency of the scaled-up Mg-MnO_2 cell decreased slightly compared to small size Mg-MnO_2 cell, which can be ascribed to the insufficient surface utilization of carbon felt in a static condition, and simple magnetic stirring or an electrolytic flow-through cell design could be employed to improve the electrochemical performance. The Mg-MnO_2 batteries were capable of lighting a blue light-emitting diode display panel when they were quickly charged at 2.8 V for only 5 min (Figure 5c). The electrochemical performance of the scaled-up Mg-MnO_2 battery reflects its huge potential for the large-scale energy storage application.

3. Conclusion

In conclusion, we have proposed and demonstrated a strategy to build up a stable solid electrolyte interface by using a solvent-in-water electrolyte for aqueous Mg-MnO_2 battery. In the solvent-in-water electrolyte, the accumulation of inorganic passivation layer on Mg anode can be greatly suppressed. Instead, a robust solid electrolyte interface composed of hybrid organic-inorganic components was formed, which was critical to stabilize the Mg anode. In addition, PEG suppressed the water activity by forming H-bond with free water, which further inhibited the decomposition of water on Mg anode. The synergistic contributions of solvent and water in the SIW electrolyte enable the Mg anode function well for aqueous Mg-MnO_2 battery. When metallic Mg anode was coupled with MnO_2 cathode in the Mn^{2+}/MnO_2 chemistry in the optimal SIW electrolyte, the fabricated Mg-MnO_2 battery achieved a high discharge voltage of ≈2.5 V, a greatly improved specific capacity of ≈500 mAh g^{-1}, and a long cycling life of over 1000 cycles. Moreover, the Mg-MnO_2 battery was demonstrated to be facilely scaled up for practical large-scale energy storage applications. The present design strategy therefore provides a promising pathway toward developing high performance aqueous Mg ion batteries with a long cycling life.

4. Experimental Section

Materials: All reagents and materials in this work were commercially available and were used without further purification. Magnesium chloride hexahydrate ($MgCl_2{\cdot}6H_2O$, ≥98.0%), manganese chloride tetrahydrate ($MnCl_2{\cdot}4H_2O$, ≥ 99.0%), sulfuric acid (H_2SO_4, 95.0–98.0%), poly(ethylene glycol) 400 (PEG 400, ≥99.9%) were purchased from Guoyao Corporation.

Mg-MnO_2 Cell Assembly: The aqueous Mg-MnO_2 battery was assembled using carbon felt (1.2 × 1.5 cm^2) as the cathode-less current collector and Mg foil as the anode. 1 M $MgCl_2$ + 1 M $MnCl_2$ in H_2O, saturated $MgCl_2$ + 1 M $MnCl_2$ in H_2O, saturated $MgCl_2$ + 1 M $MnCl_2$ in H_2O:PEG = 2:1 and saturated $MgCl_2$ + 1 M $MnCl_2$ in H_2O:PEG = 1:1 solutions with 0.0018 M H_2SO_4 were used as the electrolytes for the Mg-MnO_2 batteries. The addition of acid was favorable for the complete dissolution of MnO_2. The carbon felt was treated in air at 400 °C for 2 h before acting as a current collector. For the scaled-up Mg-MnO_2 battery, the cathode and anode of the stacked cells were separated by a plastic grid. Ti foil was used as a part of current collector to ensure good electrical conductivity for the carbon felts.

Characterizations: Powder diffraction X-ray (PXRD) patterns were collected on a Philips X'Pert PRO SUPER Xray diffractometer equipped with graphite monochromatized Cu K_α radiation. Scanning electron microscope (SEM, JEOL-6700F) was carried out to characterize the morphologies, sizes, and structures of the Mg and MnO_2. Valence state measurements were carried out by X-ray photoelectron spectroscopy (XPS) using a monochromatic Al K_{a1} source (1486.6 eV). For the XRD, SEM, and XPS measurements, the carbon felt cathodes were washed with deionized water for at least three times and dried overnight in a vacuum oven.

Electrochemical Tests: The cycling performance and rate capability of the cells were tested on a battery testing system (Landt, Wuhan, China). In the charge-discharge measurements, a constant potential 2.7 or 2.8 V with cut-off capacity was applied to the charge process of the cells, and a technique of constant current with 1.4 V cut-off potential was used in the discharge process. The CV and electrochemical impedance spectra with a frequency range of 100 kHz to 1 Hz were collected using a Biologic electrochemical workstation (VMP3, France). All electrochemical tests were conducted at room temperature.

Theoretical Calculations: First-principles calculations were performed with the CASTEP package within the generalized gradient approximation (GGA) as formulated by the Perdew–Burke–Ernzerhof (PBE) functional.[29,30] The final set of energies for all calculations was computed with an energy cut-off of 571.4 eV. A five atomic layer of Mg(002) surface was modeled with 20 Å vacuum space to avoid the interaction from the nearby layers. A cell with dimension of 20 Å × 20 Å × 20 Å was used for the calculation of the solvated magnesium ions. The convergence criteria for energy were set to be 10^{-5} eV, and the residual forces on each atom became smaller than 0.03 eV $Å^{-1}$. The Brillouin zone integration was performed with 2 × 2 × 1 and 1 × 1 × 1 Γ-centred Monkhorst-Pack k-point meshes in geometry optimization calculations. The solvent molecules adsorption energy was defined as: $E_{ads} = E_{molecule/substrate} - E_{substrate} - E_{molecule}$.

Supporting Information

Supporting Information is available from the Wiley Online Library or from the author.

Acknowledgements

The work was supported financially by the startup funding from the Fundamental Research Funds for the Central Universities (Grant KY2060000150) and China Postdoctoral Science Foundation (2021M693061). The authors at USTC acknowledge the support from USTC Center for Micro and Nanoscale Research and Fabrication and the advanced computing resources provided by the Supercomputing Center of the USTC. The authors acknowledge the useful discussion with Prof. Yan Yao and Dr. Yanliang Liang.

Conflict of Interest

The authors declare no conflict of interest.

Data Availability Statement

The data that support the findings of this study are available on request from the corresponding author. The data are not publicly available due to privacy or ethical restrictions.

Keywords

Mg anodes, Mg-MnO_2 batteries, MnO_2 cathodes, solid electrolyte interfaces, solvent-in-water electrolytes

Received: October 26, 2021
Revised: March 6, 2022
Published online:

[1] M. Armand, J. M. Tarascon, *Nature* **2008**, *451*, 652.
[2] a) J. M. Tarascon, M. Armand, *Nature* **2001**, *414*, 359; b) D. Larcher, J. M. Tarascon, *Nat. Chem.* **2015**, *7*, 19.
[3] L. Chen, L. Cao, X. Ji, S. Hou, Q. Li, J. Chen, C. Yang, N. Eidson, C. Wang, *Nat. Commun.* **2020**, *11*, 2638.
[4] X. Shan, F. Guo, D. S. Charles, Z. Lebens-Higgins, S. Abdel Razek, J. Wu, W. Xu, W. Yang, K. L. Page, J. C. Neuefeind, M. Feygenson, L. F. J. Piper, X. Teng, *Nat. Commun.* **2019**, *10*, 4975.
[5] Y.-Q. Li, H. Shi, S.-B. Wang, Y.-T. Zhou, Z. Wen, X.-Y. Lang, Q. Jiang, *Nat. Commun.* **2019**, *10*, 4292.
[6] H. Zhang, K. Ye, K. Zhu, R. Cang, J. Yan, K. Cheng, G. Wang, D. Cao, *Chem. - Eur. J.* **2017**, *23*.
[7] a) Y. Li, J. Fu, C. Zhong, T. Wu, Z. Chen, W. Hu, K. Amine, J. Lu, *Adv. Energy Mater.* **2019**, *9*, 1802605; b) D. Chao, W. Zhou, C. Ye, Q. Zhang, Y. Chen, L. Gu, K. Davey, S.-Z. Qiao, *Angew. Chem., Int. Ed.* **2019**, *58*, 7823.
[8] a) D. Chao, W. Zhou, F. Xie, C. Ye, H. Li, M. Jaroniec, S.-Z. Qiao, *Sci. Adv.* **2020**, *6*, eaba4098; b) Z. Liu, Y. Huang, Y. Huang, Q. Yang, X. Li, Z. Huang, C. Zhi, *Chem. Soc. Rev.* **2020**, *49*, 180; c) M. Liu, H. Ao, Y. Jin, Z. Hou, X. Zhang, Y. Zhu, Y. Qian, *Mater. Today Energy* **2020**, *17*, 100432.
[9] a) F. Wang, O. Borodin, T. Gao, X. Fan, W. Sun, F. Han, A. Faraone, J. A. Dura, K. Xu, C. Wang, *Nat. Mater.* **2018**, *17*, 543; b) F. Mo, G. Liang, Q. Meng, Z. Liu, H. Li, J. Fan, C. Zhi, *Energy Environ. Sci.* **2019**, *12*, 706; c) Q. Zhang, Y. Ma, Y. Lu, L. Li, F. Wan, K. Zhang, J. Chen, *Nat. Commun.* **2020**, *11*, 4463.
[10] a) L. Blanc, D. Kundu, L. Nazar, *Joule* **2020**, *4*, 771; b) J. Yi, P. Liang, X. Liu, K. Wu, Y. Liu, Y. Wang, Y. Xia, J. Zhang, *Energy Environ. Sci.* **2018**, *11*, 3075.
[11] a) C. Ling, D. Banerjee, M. Matsui, *Electrochim. Acta* **2012**, *76*, 270; b) M. Matsui, *J. Power Sources* **2011**, *196*, 7048.
[12] a) H. Dong, O. Tutusaus, Y. Liang, Y. Zhang, Z. Lebens-Higgins, W. Yang, R. Mohtadi, Y. Yao, *Nat. Energy* **2020**, *5*, 1043; b) D. Aurbach, Z. Lu, A. Schechter, Y. Gofer, H. Gizbar, R. Turgeman, Y. Cohen, M. Moshkovich, E. Levi, *Nature* **2000**, *407*, 724; c) T. Gao, M. Noked, A. J. Pearse, E. Gillette, X. Fan, Y. Zhu, C. Luo, L. Suo, M. A. Schroeder, K. Xu, S. B. Lee, G. W. Rubloff, C. Wang, *J. Am. Chem. Soc.* **2015**, *137*, 12388; d) K. A. See, K. W. Chapman, L. Zhu, K. M. Wiaderek, O. J. Borkiewicz, C. J. Barile, P. J. Chupas, A. A. Gewirth, *J. Am. Chem. Soc.* **2016**, *138*, 328.
[13] a) C. Ling, R. Zhang, *Front. Energy Res.* **2017**, *5*, 30; b) K. W. Nam, S. Kim, S. Lee, M. Salama, I. Shterenberg, Y. Gofer, J.-S. Kim, E. Yang, C. S. Park, J.-S. Kim, S.-S. Lee, W.-S. Chang, S.-G. Doo, Y. N. Jo, Y. Jung, D. Aurbach, J. W. Choi, *Nano Lett.* **2015**, *15*, 4071.
[14] a) C.-S. Li, Y. Sun, F. Gebert, S.-L. Chou, *Adv. Energy Mater.* **2017**, *7*, 1700869; b) Y. Xue, H. Miao, S. Sun, Q. Wang, S. Li, Z. Liu, *J. Power Sources* **2015**, *297*, 202.
[15] Y. Yamada, in *Anion Exchange Membrane Fuel Cells: Principles, Materials and Systems*, (Eds.: L. An, T. S. Zhao), Springer International Publishing, Cham **2018**, p. 141.
[16] C. Li, F. Cheng, W. Ji, Z. Tao, J. Chen, *Nano Res.* **2009**, *2*, 713.
[17] a) D. Marx, M. E. Tuckerman, J. Hutter, M. Parrinello, *Nature* **1999**, *397*, 601; b) Y. Wang, T. Wang, D. Dong, J. Xie, Y. Guan, Y. Huang, J. Fan, Y.-C. Lu, *Matter* **2021**, *5*, 162.
[18] M. E. Tuckerman, D. Marx, M. Parrinello, *Nature* **2002**, *417*, 925.
[19] L. Cao, D. Li, E. Hu, J. Xu, T. Deng, L. Ma, Y. Wang, X.-Q. Yang, C. Wang, *J. Am. Chem. Soc.* **2020**, *142*, 21404.
[20] Y. Jin, K. S. Han, Y. Shao, M. L. Sushko, J. Xiao, H. Pan, J. Liu, *Adv. Funct. Mater.* **2020**, *30*, 2003932.
[21] a) L. Suo, O. Borodin, T. Gao, M. Olguin, J. Ho, X. Fan, C. Luo, C. Wang, K. Xu, *Science* **2015**, *350*, 938; b) L. Suo, O. Borodin, W. Sun, X. Fan, C. Yang, F. Wang, T. Gao, Z. Ma, M. Schroeder, A. von Cresce, S. M. Russell, M. Armand, A. Angell, K. Xu, C. Wang, *Angew. Chem., Int. Ed.* **2016**, *55*, 7136.
[22] a) K. Shimokawa, T. Atsumi, N. L. Okamoto, T. Kawaguchi, S. Imashuku, K. Wagatsuma, M. Nakayama, K. Kanamura, T. Ichitsubo, *Adv. Mater.* **2021**, *33*, 2007539; b) Z. Zhao-Karger, R. Liu, W. Dai, Z. Li, T. Diemant, B. P. Vinayan, C. Bonatto Minella, X. Yu, A. Manthiram, R. J. Behm, M. Ruben, M. Fichtner, *ACS Energy Lett.* **2018**, *3*, 2005; c) L. Chen, J. L. Bao, X. Dong, D. G. Truhlar, Y. Wang, C. Wang, Y. Xia, *ACS Energy Lett.* **2017**, *2*, 1115.
[23] A. Ansari, A. Ali, M. Asif, Shamsuzzaman, *New J. Chem.* **2018**, *42*, 184.
[24] I. A. Taub, W. Roberts, S. LaGambina, K. Kustin, *J. Phys. Chem. A* **2002**, *106*, 8070.
[25] a) Y. Lu, W. Zhang, X. Li, S. Xu, *RSC Adv.* **2017**, *7*, 31628; b) S. Ma, W. Liu, Z. Wang, C. Hu, C. Tang, *Polym.-Plast. Technol. Eng.* **2010**, *49*, 467.
[26] F. Wang, O. Borodin, M. S. Ding, M. Gobet, J. Vatamanu, X. Fan, T. Gao, N. Eidson, Y. Liang, W. Sun, S. Greenbaum, K. Xu, C. Wang, *Joule* **2018**, *2*, 927.
[27] Y. Bourlier, M. Bouttemy, O. Patard, P. Gamarra, S. Piotrowicz, J. Vigneron, R. Aubry, S. Delage, A. Etcheberry, *ECS J. Solid State Sci. Technol.* **2018**, *7*, P329.
[28] a) W. Chen, G. Li, A. Pei, Y. Li, L. Liao, H. Wang, J. Wan, Z. Liang, G. Chen, H. Zhang, J. Wang, Y. Cui, *Nat. Energy* **2018**, *3*, 428. b) B. Delley, *J. Phys. Chem.* **1990**, *92*, 508.
[29] S. J. Clark, M. D. Segall, C. J. Pickard, P. J. Hasnip, M. I. J. Probert, K. Refson, M. C. Payne, *Z. Kristallogr.- Cryst. Mater.* **2005**, *220*, 567.
[30] P. E. Blochl, *Phys. Rev. B* **1994**, *50*, 17953.